Applied Thermal Engineering 213 (2022) 118660

Contents lists available at ScienceDirect

Applied Thermal Engineering

journal homepage: www.elsevier.com/locate/apthermeng

Research Paper

Designing a novel small-scale parabolic trough solar thermal collector with secondary reflector for uniform heat flux distribution

S. Shajan [a,b,*], V. Baiju [a]

[a] Energy Research Lab, Department of Mechanical Engineering, TKM College of Engineering, Kollam, Kerala, India
[b] APJ Abdul Kalam Technological University, Kerala, India

ARTICLE INFO

Keywords:
Parabolic trough solar collector
Secondary reflector
Ray tracing
Response surface
Computational analysis

ABSTRACT

This paper presents a new stepwise approach to design a medium-temperature solar parabolic trough collector with a secondary reflector, which is the fastest growing technology among concentrated solar power technology. The goal of the design is to have a homogeneous concentrated solar flux distribution with maximal output power over the receiver tube. Tonatiuh, a Monte Carlo ray-tracing based optical simulation software, has been used to conduct the ray-tracing analysis of the secondary reflector. Response surface methodology has been used to examine and select the desirable configuration of the solar collector system, and the findings have been analysed using the analysis of variance. It is found that the use of secondary reflector improves the uniformity of heat flux distribution to 0.58, whereas it is 1.0836 for the solar collector without the secondary reflector. For a target output power of 5.5 kW, the most attractive configuration has a maximum desirability value of 0.974. The computational fluid dynamics analysis has been performed in the configuration with better uniform heat flux and the collector without a secondary reflector, using the flux distribution acquired from the ray-tracing analysis. Results show that the use of secondary reflector significantly reduces the thermal gradient, and the heat flux distribution is found to be homogenous. By determining configurations with the best heat flux distribution against a specific output power, the approach provided in this paper lays the groundwork for future research on the design of parabolic trough solar collector systems with secondary reflectors.

1. Introduction

Solar thermal energy conversion systems are now regarded as one of the most promising future power generation alternatives to fossil fuel power plants, which emit greenhouse gases and contribute to global warming. Parabolic Trough Collectors (PTCs) are the proven solar collector technology for medium temperature applications, i.e. up to 400 °C [1,2,3,4]. The parabolic trough reflector and receiver tube are the two critical components of conventional PTCs based on Concentrated Solar Power (CSP) technology [5], as illustrated in Fig. 1. In conventional PTCs, solar radiation is concentrated on the lower periphery of the receiver tubes, while the remainder of the surface receives direct solar radiation. This results in a non-uniform distribution of heat flux around the receiver tube's circumference [6,7,8].

The non-uniform heat flux distribution in the parabolic trough receiver poses significant challenges to the performance of the PTCs. These include the following: (i) the non-uniform heat flux distribution around the absorber wall causes the receiver to deflect away from the parabolic trough's focal axis, lowering the system's optical efficiency [9]. (ii) the local peak temperature caused by the non-uniform heat flux may deteriorate the spectral selective coating on the evacuated absorber tube surface, lowering the spectral concentration and increasing heat and vacuum loss due to hydrogen permeation. Thus, it is obvious that the non-uniform distribution of heat flux should be kept below safe levels to ensure a long service life for the receiver tube. Despite the fact that numerous investigations were conducted, the majority of heat transfer investigations on the receiver tubes presented overlooked the effects of uneven heat distribution on the heating element's surface. They presupposed a uniform distribution of heat flux around the absorber tube surface [10,11,12]. Solar heat flux distributions over the PTC receiver tubes, which are non-uniform, are rarely investigated. Many studies carried out based on the Monte Carlo ray tracing (MCRT) technique revealed that the heat flux on the receiver tube of a PTC is highly non-uniform. The most important investigations are the investigations of Kulahli et al. [13], Wang et al. [14], and Zou et al. [15]. Mitigating non-uniformity in concentrated flux distributions is a critical area of research in which researchers are particularly interested.

* Corresponding author.
E-mail addresses: shajan@sctce.ac.in (S. Shajan), baiju@tkmce.ac.in (V. Baiju).

https://doi.org/10.1016/j.applthermaleng.2022.118660
Received 10 October 2021; Received in revised form 27 March 2022; Accepted 13 May 2022
Available online 18 May 2022

Nomenclature

C_p	Specific heat capacity, (J/kg·K)
D	Diameter of the receiver tube (m)
f_p	Focal length of the primary collector (m)
f_s	Focal length of the secondary reflector (m)
f'	Distance to receiver centre from the focal point (m)
G_k	Production rate of k (kg/m·s^3)
G_ε	Production term in ε equation (kg/m·s^4)
g_i	Gravitational acceleration (m/s^2)
k	Turbulence kinetic energy (m^2/s^2)
L	Length of the collector (m)
S_T	Energy source term (W/m^3)
S_k, S_ε	User-defined source terms
T	Temperature (K)
t	Time (s)
u	Velocity in x direction (m/s)
W_a	Aperture width of the primary collector (m)
W_p	Half aperture of the primary reflector (m)
Ws	Half-width of the secondary reflector (m)
W_s	Width of the secondary reflector (m)
Y_k	Contribution of fluctuating dilatation (kg/m·s^3)
Y_ε	Destruction term of turbulent dissipation (kg/m·s^4)

Greek symbols

θ	Radial angular displacement (mrad)
λ	Thermal conductivity (W/m·K)
ρ	Density (Kg/m^3)
μ	Dynamic viscosity (kg/m·s)
μ_t	Turbulent viscosity (kg/m·s)
ε	Turbulent dissipation rate (J/kg·s)
ϕ_{rp}	Rim angle of the primary collector (°)
ϕ_{rs}	Rim angle of secondary collector (°)
γ	Function of circumsolar radiation
χ	Function of circumsolar radiation
δ_{ij}	Intermolecular distance
σ	Surface tension (kg/m)
σ_k	Turbulent Prandtl number for k
σ_ε	Turbulent Prandtl number for ε

Abbreviations

CCD	Central Composite Design
CFD	Computational Fluid Dynamics
CSP	Concentrated Solar Power
DoE	Design of Experiments
HTF	Heat Transfer Fluid
PTC	Parabolic Trough Collector
RSM	Response Surface Methodology

Literature reveals the use of various heat transfer enhancement technologies to control the non-uniform heat flux distribution in the receiver tube of PTCs [16,17,18]. Many of these concepts, such as modified absorber geometry and objects inside the flow such as dimples, inserts, fins, and protrusions, have enhanced the temperature gradient over the receiver tube surface. Ghasemi and Ranjbar [19] tried porous rings to improve heat transfer in the receiver tube. They found that the porous ring receiver tube's heat transfer characteristics were higher than the porous fin and solid fin receivers. Other studies about the thermal performance of partially [20] and fully filled porous media [21] in receiver tubes also demonstrated that the temperature gradient could be minimised considerably by using the porous media.

On the other hand, researchers have recently investigated a secondary reflector as part of PTC assembly, which enhances the collector's optical efficiency by distributing the flux around the receiver with maximum total heat. This configuration increases the collector's optical efficiency by balancing the flux distribution around the receiver with the highest total heat output [22,23]. One of the most notable benefits of this approach is that it does not affect the flow, whereas other techniques impose the flow pressure drop, which leads to pumping power penalty. The studies demonstrate that using a secondary reflector in the PTC reduces the end losses and increases the concentration ratio [24,25]. Abdelhamid et al. [26] investigated a PTC with a compound parabolic booster reflector and reported an outlet temperature of 638 K. Wang et al. [9] conducted a study on secondary reflectors and reported that the use of secondary reflector improves the temperature uniformity across the receiver circumference with 4% reduction in collector efficiency.

Rodriguez and Rosengarten [27] investigated flat plate secondary reflectors for PTCs with longer focal lengths and an 80° rim angle. They found that the collector's concentration ratio increased by approximately 80%. Minaeian et al. [28] numerically investigated and optimised various geometric parameters of secondary reflectors in terms of flux density and flux uniformity. They compared optical properties of circular, flat, few segmented, and parabolic secondary reflectors. They proved that a few flat segmented collectors could boost heat flux to 87.9%, while parabolic secondary reflectors provided the best flux uniformity. Bellos and Tzivandis [23] proposed a vertical booster reflector mounted on the longitudinal edge of the trough to reduce end

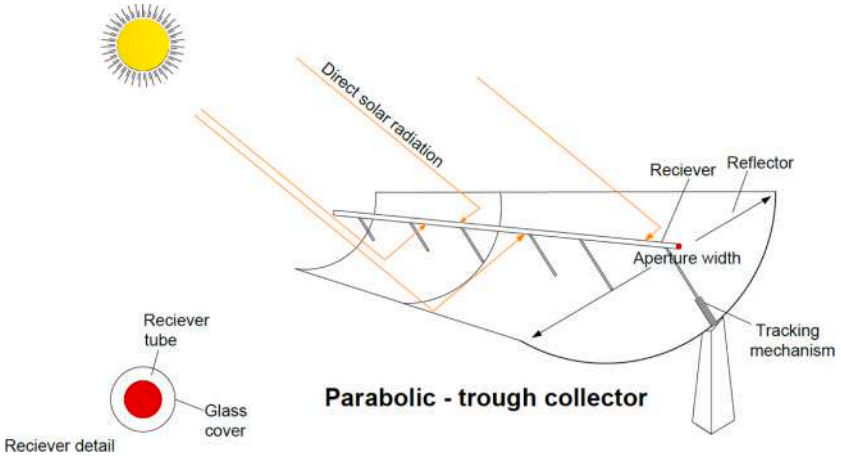

Fig. 1. Schematic of a conventional parabolic trough collector.

losses and make use of the additional irradiation that falls directly on it. Tang et al. [29] presented a theoretical design aspect of a segmented broken-line mirror type secondary reflector for PTCs. The edge ray and stepwise flux compensation strategy were used to balance the heat flux by adjusting the position of the receiver. Hack, Zhu, and Wendelin [30] proposed a novel adaptive approach for optimising the shape of secondary reflector, and the resulting design outperforms other secondary reflector designs. Balaji et al. [31] carried out an optical analysis of a parabolic and an involute secondary reflector used in a linear Fresnel collector. They discovered that the parabolic profile had a 2.83% increase in optical efficiency over the involute reflector. Bharti et al. [22] investigated a parabolic secondary reflector experimentally and observed an increase in the working fluid outlet temperature. The results indicated that a parabolic secondary reflector increased the maximum thermal efficiency of a PTC by 6.5% over a PTC without a secondary reflector.

The literature review indicates that further investigation of the use of a secondary reflector to homogenise the heat flux distribution over the receiver tube is necessary to improve the system's performance. The position of the receiver tube with respect to the primary collector's focal axis, as well as the position and size of the parabolic secondary reflector, are the most critical parameters affecting the optical and thermal performance of these PTCs. Without careful design, the use of a secondary reflector can result in a more severe non-uniform heat flux distribution than a conventional collector and even structural failure of the receiver tube. This demonstrates the critical nature of a properly designed parabolic trough collector with a secondary reflector for the solar collector's reliability and long service life. The effect of receiver tube position and secondary reflector width on heat flux distribution is analysed in this study, and the optimal values for a targeted output power are proposed. This paper also discusses the characteristics and models of MCRT, as well as the models and assumptions used in the Design of Experiment (DoE) and Response Surface Methodology (RSM). Additionally, a numerical analysis using Computational Fluid Dynamics (CFD) is performed to determine the effect of the improved heat flux distribution on the temperature field of the receiver tube wall and the heat transfer fluid (HTF). This article proposes a detailed new design approach for a PTC that incorporates a secondary parabolic reflector for homogenising the concentrated solar flux distribution on the receiver tube in order to achieve a uniform flux distribution with the desired total output power.

2. Methodology

The optimal configuration of a PTC with a secondary reflector is designed in two stages. MCRT analysis is performed during the first phase to study the flux distribution around the receiver tube surface and predict the power output for various configurations considered. The design points for the PTC configurations are developed using a classical DoE approach based on central composite design (CCD). The MCRT-based optical simulation software, Tonatiuh is used for ray-tracing analysis. In the second phase, response surface methodology (RSM) is used to investigate the effect of the receiver tube and a secondary reflector configuration on the power output and heat flux distribution of the PTC system. The ANOVA (Analysis of Variance) procedure is used to determine the significance and adequacy of the mathematical models developed by RSM to describe the relationship between PTC system parameters and outputs. Additionally, a random ray-tracing analysis is performed to validate the MCRT and DoE results. Furthermore, a desirability functional analysis is performed to determine the system's optimal configuration for optimum heat flux uniformity without compromising the total power. The temperature distribution across the HTF and the pipe is evaluated using ANSYS Fluent 2020 R1. The study compares PTC without a secondary reflector to PTC with the most desirable parameters. The addition of a secondary reflector results in a shadowing effect, which may have an effect on the heat transfer fluid's temperature. As a result, the average temperature of the fluid, absorber surface temperature uniformity and thermal efficiency is sought for comparison. The methodology is summarised in Fig. 2.

2.1. Parameters of the primary concentrator and the receiver tube

The PTC selected for the study is detailed in Table 1. It is identical to the one currently in use at Energy Research Lab, TKM College of Engineering, Kollam, Kerala, India. The PTC has a stainless steel concentrator and a bare receiver tube (copper). The original PTC is ideal for applications that requires a 5.5 kW heating system. The parameters of the parabolic trough and receiver tube of the PTC system used in this study are shown in Fig. 3. The PTC geometry is determined by the following parameters: a 70° rim angle and a 1 m focal length of the parabola without glass cover.

The physical characteristics of the system are determined using the following equations [32].

The aperture of a parabola is a function of the focal length and rim angle as,

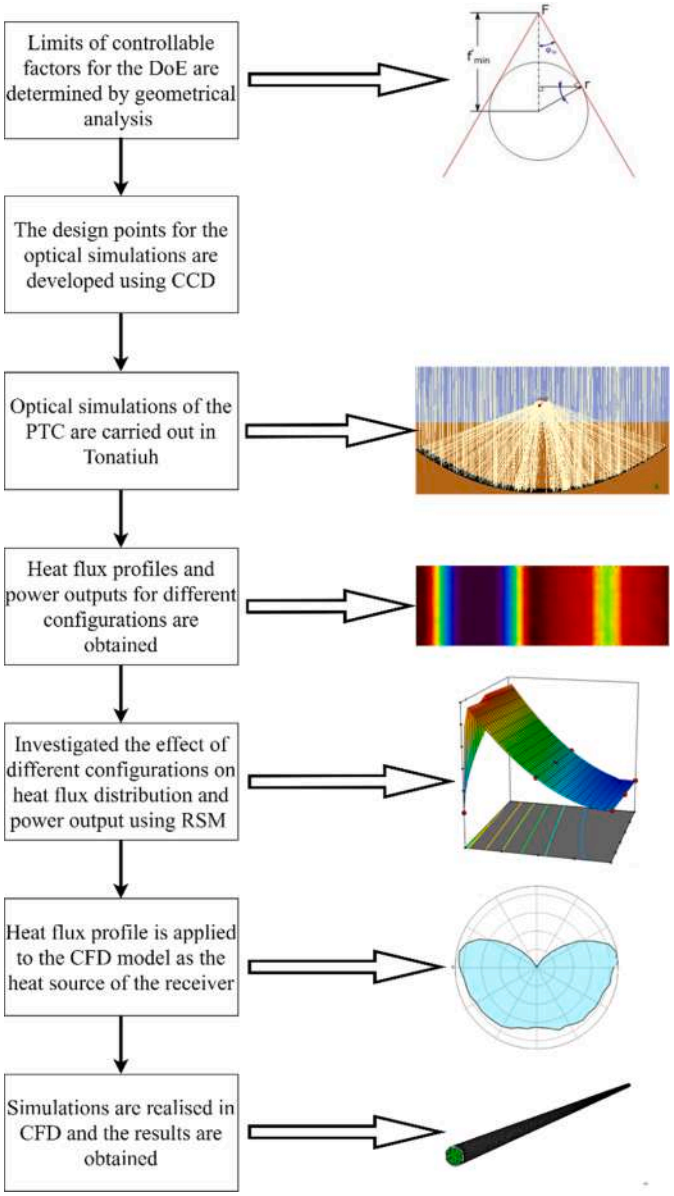

Fig. 2. Summary of the procedure.

Table 1
Physical parameter of the primary collector and receiver.

Item	Numerical value
Aperture area of the collector	7 (m^2)
Aperture width (W_a)	2.8 (m)
Collector length (L)	2.5 (m)
Focal distance (f)	1 (m)
Rim angle (φ_r)	70°
Diameter of the receiver (D)	0.02665 (m)
Thickness of the receiver	0.00165 (m)
Geometric concentration ratio	33
Receiver tube absorptivity	0.98
Concentrator reflectivity	0.98

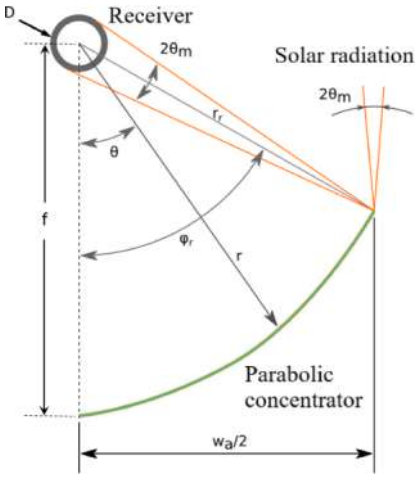

Fig. 3. Parameters of a PTC.

$$W_a = 4ftan\frac{\varphi_r}{2} \tag{1}$$

where the radius of the parabola at the rim angle corresponding to the focal length is

$$r_r = \frac{2f}{1+cos\varphi_r} \tag{2}$$

The optimum diameter of the receiver tube can be related to the incident angle as,

$$D = 2r_r sin\theta_m \tag{3}$$

However, Eq. (3) is valid for perfect reflectors without profile and fabrication errors. Furthermore, the equation assumes that the beam radiation hits normal (zero incidence angle) to the concentrator surface. Besides, considering the possible deformations of the 2.5 m long absorber tube with simple supporting structure, and the pressure losses at smaller absorber diameters, the commercially available absorber tube with 0.02665 m is considered for this study. With this, the geometric concentration ratio of the concentrator can be expressed as,

$$C_c = \frac{sin(\varphi_r)}{\pi sin(\theta_m)} = \frac{W_a L}{\pi DL} \tag{4}$$

where θ_m is the half-angle subtended by the Sun on the Earth.

2.2. Parameters of secondary reflector and design of experiment

The absorber tube is positioned at the focal axis in conventional PTCs, as illustrated in Fig. 4b. Under ideal conditions, the entire concentrated radiations should be intercepted on the bottom periphery of the tube surface along the rim angle. However, in practice, because the top periphery is exposed to direct solar radiation, the receiver experiences a non-uniform heat flux. When the absorber tube is positioned above the collector's focal axis, the majority of the concentrated radiations are intercepted by the tube's small surface area, as illustrated in Fig. 4a. This increases the circumferential temperature gradient and, as a result, the thermal stress on the receiver tube [22]. When the absorber tube is positioned below the concentrator's focal axis (see Fig. 4c), heat flux is distributed over a larger surface area, but a portion of the reflected radiations are lost.

Typically, the intercept factor is used to estimate the concentrator's imperfections. The intercept factor is defined as the ratio of solar insolation intercepted by the receiver to that reflected by the collector (concentrator). The expression of the intercept factor for an absorber extends from A to B is given in Eq.(5) [33]. A small deviation of the receiver tube from the focal axis results in a larger change in the intercept factor [34]. The intercept factor decreases as the deviation increases when the receiver is mounted below the exact focal axis. However, by employing a secondary reflector, the majority of the escaped rays on the receiver tube are re-intercepted. A simple method of homogenising the heat flux over the periphery is to install the receiver tube below the focal axis of the primary collector and a secondary

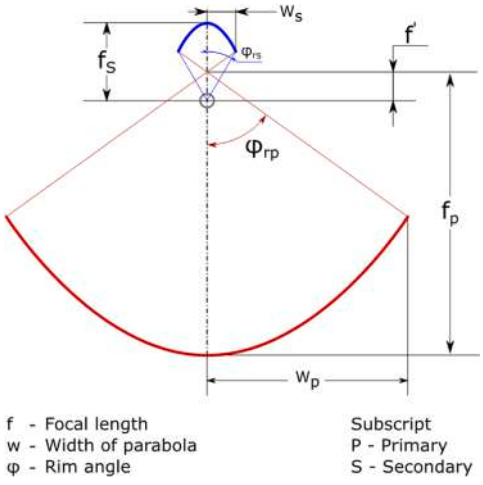

Fig. 5. Schematic diagram of a PTC with secondary booster reflector.

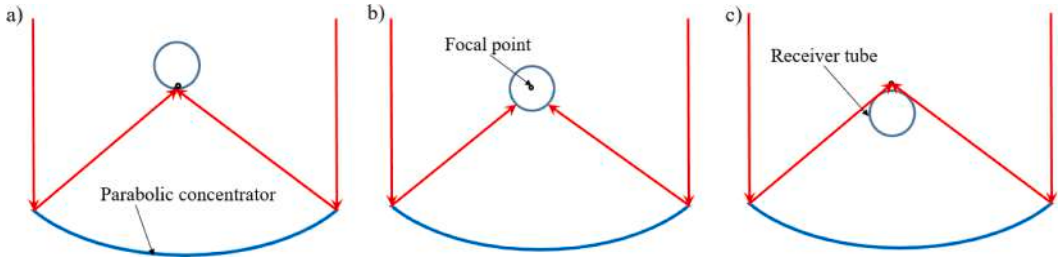

Fig. 4. Receiver tube positions (a) above focal axis (b) at the focal axis (c) below the focal axis.

reflector above the tube [35]. The schematic diagram of a PTC with a secondary booster reflector is shown in Fig. 5.

$$Interceptfactor = \frac{\int_A^B I_R(R)dR}{\int_{-\infty}^{+\infty} I_R(R)dR} \tag{5}$$

where R is the radius of the receiver in meters, and I_R is the radiation reflected from the concentrator in W/m^2.

The design points are derived from a CCD with two factors and two levels. CCD is a collection of statistical and mathematical techniques for establishing a series of design points that will yield adequate response predictions. To begin, a geometric study is conducted to determine the minimum and maximum locations of the absorber tube ($f^{`}$) relative to the focal axis of the primary collector. Additionally, the study establishes the aperture (*W-s*) limits of the secondary reflector for the purpose of designing experiments to perform desired analyses. The absorber's minimum distance from the primary reflector's focal axis is determined by the position of the rays reflected from the outer edge of the aperture rendered tangential to the tube, as illustrated in Fig. 6a. The maximum limit is calculated by assuming that at least 50% of reflected rays intercept the receiver tube, as illustrated in Fig. 6b. The maximum and minimum values can be calculated using Eq. (5), which can be found in Fig. 6a and b.

$$f^{`} = \frac{r}{\sin\varphi_{rp}} \tag{6}$$

where $\varphi_{rp} = 70^{\circ}$ for the minimum limit and $\varphi_{rp} = 19.29^{\circ}$ for the maximum limit for this configuration as obtained from the trigonometry. The secondary reflector's minimum width is limited by the diameter of the receiver tube. The maximum aperture of the secondary reflector is limited to 5% of the aperture of the primary reflector, as a large secondary reflector width is superfluous and results in significant optical loss due to the shading effect. As illustrated in Table 2, these limits are used to design ray-tracing analyses to determine the secondary reflector's effect on the distribution of heat flux around the receiver and total power.

2.3. MCRT model of PTC

Ray-tracing analysis is critical for the geometric and optical design of CSP systems because it affects their optical and thermal performance and enables more detailed test results with fewer experimental requirements [36]. The MCRT method is an efficient approach for evaluating the optical performance of concentrating solar collectors. Based on the collector configurations, as shown in Table 1 and receiver position ($f^{`}$) and secondary reflector configurations (*Ws*) obtained through CCD (Table 3), thirteen design points are identified.

The major challenge in the optical analysis of a solar-based system is identifying the optimum model for the Sun. Fig. 7 illustrates a comparison of normalised intensity as a function of angular displacement from the centre for the various sunshape models. The limb-darkened solar disc with circumsolar radiation produces the most realistic sunshape because it incorporates the effects of interaction with the Earth's atmospheric particles. The Neumann and Buie models are the most frequently used limb-darkened solar disc models.

Tonatiuh is a cutting-edge open-source ray-tracing software developed by Spain's National Renewable Energy Centre (CENER) to design and analyse CSP systems. Tonatiuh provides the Buie sunshape, the most realistic and widely used model of the solar disc with limb-darkened limbs and circumsolar radiation [37]. The system's geographical location has no bearing on this model, which exhibits both axial and central symmetry. The distribution of the rate of energy per unit solid angle in a specified direction and per unit projected surface area normal to the specified direction can be calculated using this model [38] as,

$$\widehat{L}_{Biue}(\theta) = \begin{cases} \dfrac{cos326(\theta)}{cos308(\theta)}, \wedge 0 \le \theta \le \theta_{disk} \\ e^{\kappa}\left(10^3\theta\right)^{\gamma}, \wedge \theta_{disk} < \theta \le \theta_{aureole} \end{cases} \tag{7}$$

where θ is the radial angular displacement, κ and γ the functions of circumsolar ratio (χ) and are expressed as.

$$\gamma = 2.2ln(0.52\chi)\chi^{0.43} - 0.1 \tag{8}$$

$$\kappa = 0.9ln(13.5\chi)\chi^{-0.3} \tag{9}$$

In optical simulations, the annual averaged angular width of the solar disk is taken as $\theta_{disk} \approx 4.65$ mrad, and the angular extent of the aureole considered is $\theta_{aureole} \approx 43.6$ mrad.

In this investigation, the reflectivity of the primary and secondary concentrators and the absorptivity of the receiver are assumed to be 0.98. Each ray tracing run considers samples of 2 million rays with an irradiance of 1 kW/m^2. The rays are chosen based on the results of the ray independent test shown in Fig. 8. The number of rays used varies between 1000 and 10,000,000, and the MCRT analysis is performed accordingly. Using a log plot, the total power is plotted against the number of rays in Fig. 8. As can be seen, the total power varies by only 0.05 percent beyond 2 million rays.

2.3.1. Modelling paradigm

Tonatiuh's computational structure is based on two models: one for incoming solar radiation and another for the radiation's interaction with the surface. The vector of the Sun's direction is defined as a function of

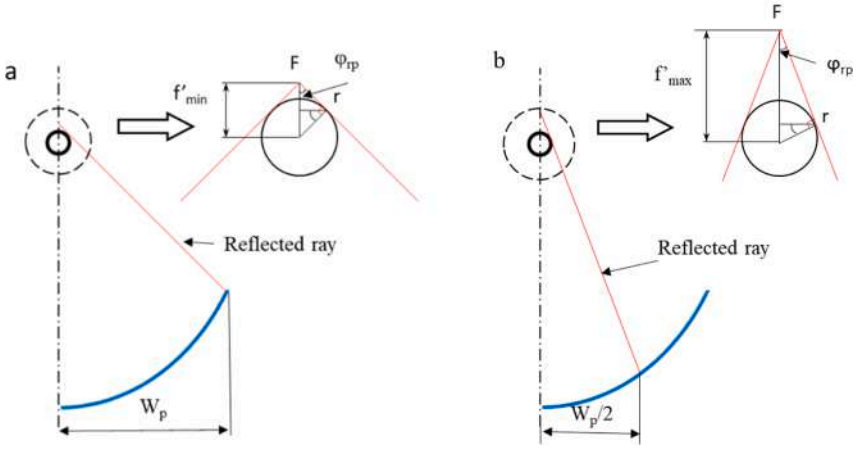

Fig. 6. Geometry to determine the location of the receiver tube (a) minimum limit, (b) maximum limit.

Table 2
Coded levels of experimental design.

Factors	Variables	Unit	Type	Low coded	High coded	Low actual	High actual
A	f	mm	Numeric	−1	+1	14.2	42
B	W-s	mm	Numeric	−1	+1	26.650	140

Table 3
Experimental configurations for ray tracing.

Exp. no.	f (mm)	W-s (mm)	$f_p - f$ (mm)	φ_{rs}(rad)	f_s (mm)	W_s (mm)
1	14.2	140	985.8	1.05512568	60.071	70
2	28.1	83.325	971.9	0.766543956	51.663	41.6625
3	28.1	83.825	971.9	0.766543956	51.663	41.6625
4	42.0	26.650	958.0	0.277101669	47.779	13.325
5	14.2	83.325	985.8	0.95685326	40.167	41.6625
6	28.1	26.650	971.9	0.384295257	34.246	13.325
7	28.1	83.325	971.9	0.766543956	51.663	41.6625
8	28.1	83.325	971.9	0.766543956	51.663	41.6625
9	28.1	83.325	971.9	0.766543956	51.663	41.6625
10	42.0	83.325	958.0	0.62981096	63.95	41.6625
11	42.0	140	958.0	0.803741478	82.353	70
12	28.1	140	971.9	0.917512604	70.864	70
13	14.2	26.650	98.58	0.610375955	21.149	13.325

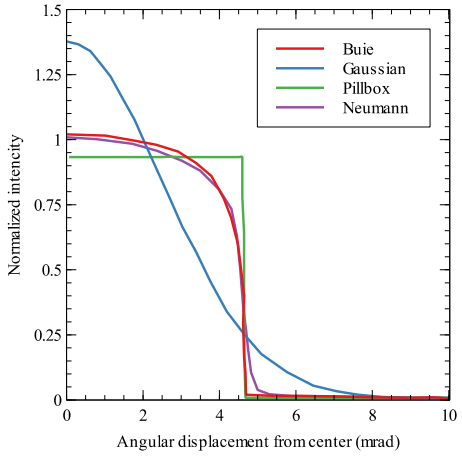

Fig. 7. Comparison of different sunshapes used in optical simulation.

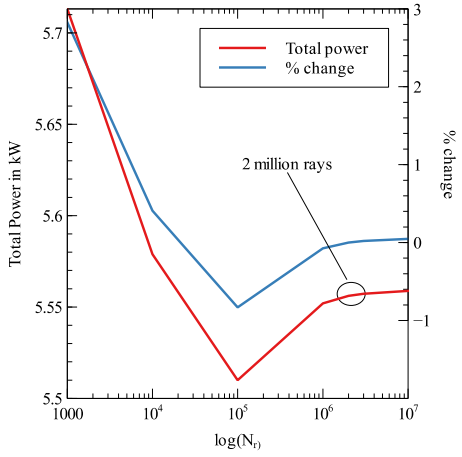

Fig. 8. Ray independent study.

four variables: latitude, declination, hour angle, and solar azimuth angle. Geometrical optics is used to determine the interaction between the incoming radiation and the surface. In Tonatiuh, the input solar flux will be mathematically transformed into a probability density function. This is accomplished through the use of the MCRT algorithm.

The optical modelling is carried out with the following assumptions:

(i) Only direct radiation is considered.
(ii) Buie sunshape is considered for modelling the Sunshape.
(iii) Solar irradiation is considered as parallel beams.
(iv) All the properties considered are independent of wavelength and beam direction.
(v) The reflective surface considered are perfectly specular without any deformation.
(vi) The tracking error of the receiver tube is not considered.

2.4. Computational Fluid Dynamic (CFD) analysis

The effect of heat flux distribution over the receiver and the heat transfer to the HTF has been numerically investigated by CFD analysis. Two 3D steady-state conjugate heat transfer CFD models are performed using the Ansys Fluent 2020 R1: one for the receiver without a secondary reflector and one for the receiver with a secondary reflector in the most desirable position. The following are the general governing equations for the incompressible HTF flow in the receiver tube [39]:

Continuity equation

$$\frac{\partial u_j}{\partial x_i} = 0 \tag{10}$$

Momentum equation

$$\rho \frac{\partial (u_i u_j)}{\partial x_i} = \frac{\partial}{\partial x_j}\left[-\rho \delta_{ij} + \mu \left(\frac{\partial u_i}{\partial x_j} + \frac{\partial u_j}{\partial x_i} \right) \right] + \rho g_i \tag{11}$$

Energy equation

$$\rho \frac{\partial (u_i C_p T)}{\partial x_i} - \frac{\partial}{\partial x_j}\left(\lambda \frac{\partial T}{\partial x_j} \right) = S_T \tag{12}$$

S_T represents the source term. Due to the incompressible nature and the absence of internal heat generation, the source term is considered zero. For the solid domain (the pipe), the first term in the energy equation is not relevant as it contributes to the convection of temperature. At the boundary nodes, the boundary heat flux contributes the source term. For modelling the effect of turbulence in HTF, two equation-based realisable k-ε turbulent models with standard wall function are used. This model solves for two equations, one for turbulent kinetic energy and another specific dissipation rate for evaluating the Reynolds stress terms. These equations are as follows:

Turbulence kinetic energy (k) equation:

$$\rho \frac{\partial (k u_j)}{\partial x_j} = \frac{\partial}{\partial x_j}\left[\left(\mu + \frac{\mu_t}{\sigma_k} \right) \frac{\partial k}{\partial x_j} \right] + G_k - Y_k + S_k \tag{13}$$

Specific dissipation (ε) equation:

$$\rho \frac{\partial (\varepsilon u_j)}{\partial x_j} = \frac{\partial}{\partial x_j}\left(\left(\mu + \frac{\mu_t}{\sigma_\varepsilon} \right) \frac{\partial \varepsilon}{\partial x_j} \right) + G_\varepsilon - Y_\varepsilon + D_\varepsilon + S_\varepsilon \tag{14}$$

The governing equations are discretised using the finite volume based Fluent solver. The 3D geometry representing the PTC receiver's models are discretised for optimum grid sizes in Ansys Fluent meshing.

The Second-order Upwind scheme is used to discretise the convection term in all the equations mentioned above, while the least square gradient scheme is used to approximate the gradient terms. The coupled algorithm is used to solve the discrete equations. Water is used as the HTF, and copper is used as the material for the pipe. The fluid velocity of 0.1 m/s and a temperature of 300 K is used as the inlet boundary condition. Since the analyses are carried out at normal atmospheric pressure, the useful working temperature of water is selected as 303–368 K. The outlet is set to be at a zero-pressure gradient and the operating pressure selected is the ambient pressure. The actual distribution of heat flux obtained through the MCRT analysis is converted to a profile file and applied as the receiver wall's thermal boundary condition for the CFD analysis. The ambient temperature is taken as 300 K.

Four different grid qualities selected are course grid, medium grid, fine grid and finer grid. A uniform heat flux of 33 kW/m^2 and the temperature along the axial direction is assumed for the analysis. The energy losses happening from the solar irradiation to the useful heat gain in the receiver tube is categorized as either optical loss or thermal loss. Two distinct thermal loss modes that occur at the receiver tube are convection and radiation loss. Optical losses are due to the imperfections in the reflector surface and its geometry. It is typically estimated using the intercept factor, which represents the fraction of direct solar radiation that reaches the receiver tube concerning the reflected radiation from the concentrator mirror. The various factors considered for providing the optical loss are given in Table 4.

A user-defined function is developed to include the optical and thermal losses mentioned here. The CFD results have all the sources of losses applicable to the receiver tube without a cover tube.

A fine mesh having 350 thousand elements is selected for the study. Fig. 9 shows the log plot for the fraction of deviation from the chosen grid with grid size tested. It is evident that the fine and finer grid's deviation is insignificant compared to the computational cost. In contrast, the deviation is significant with medium and coarse meshes considered.

2.5. Validation of the proposed models

Due to the lack of measured flux distributions around the demonstrative receiver tubes, the proposed methodology for ray tracing is validated using Jeter's analytical model [7]. The receiver tube chosen in Jeter's study has a geometrical concentration ratio of 20 and a 90° rim angle corresponding to LS2 and LS3. A uniform Sun with an angular radius of 7.5 mrad is assumed to be the source with a DNI of 1 kW/m^2. The local concentration ratio (LCR) obtained from the ray-tracing analysis is plotted in Fig. 10 in relation to the angular location between 0 and 180°. The figure clearly shows that a maximum deviation of 1.15 percent exists beyond the angular location of 120°. However, the deviation is negligible in places where the flux value is significant. Additionally, the current model overestimates the effect of shading when compared to the Jeter profile.

Similarly, with the grid size selected, a CFD analysis is performed by varying the inlet velocity with the heat flux kept constant for verifying the validity of the CFD model. Three different inlet velocities (0.1 m/s, 0.25 m/s and 0.5 m/s) are used to analyze the model. The velocities correspond to transition flow and turbulent flow. The results are then compared with Gnielinski modification of the Petukhov–Popov formula for Nusselt number as explained by Abraham et al. [40] and is presented in Table 5. The maximum deviation between the numerical analysis and correlation obtained is only 2.174%. The deviation is within an acceptable range.

Table 4
Optical errors considered in the present study.

Sl. no	Parameter (λ_i)	Numerical value
1	Shadowing factor	0.97
2	Tracking error	0.95
3	Collector mirror imperfection	0.96
4	Mirror cleanliness	0.93
4	Miscellaneous factors	0.95
5	Shading factor	0.96

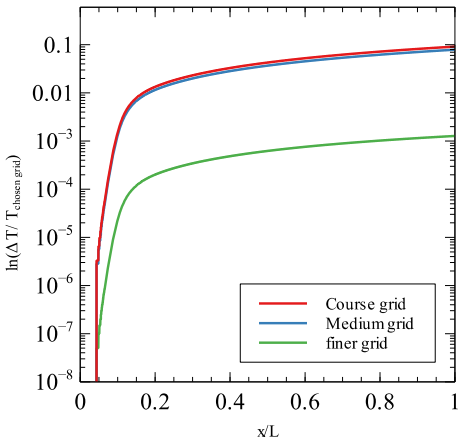

Fig. 9. Grid convergence test.

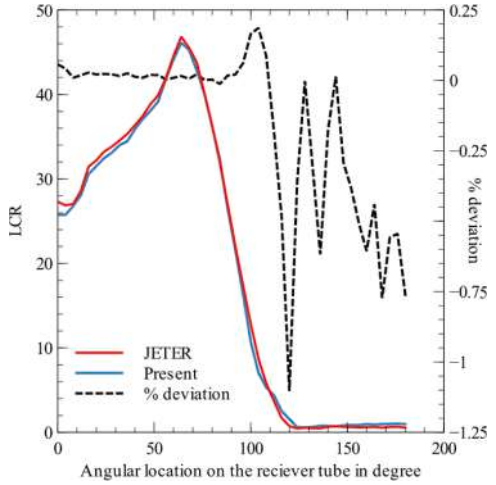

Fig. 10. Comparison of LCR profile for a round receiver tube.

Table 5
Validation of numerical study.

u (m/s)	0.1	0.25	0.5
Re	2646.025	6615.0625	13230.125
$Nu_{calculated}$	15.88	55.1656	105.7268
Nu_{CFD}	15.34	53.976	103.802
% deviation	2.174	2.156	1.823

3. Results and discussion

3.1. Ray tracing and heat flux analysis

The concentrator, receiver and secondary reflector parameters as illustrated in Tables 1 and 3 are used in the Tonatiuh simulations. Fig. 11a demonstrates the rays' path reflected by the collector on the receiver tube when the tube is mounted at the focal axis. The bottom half of a conventional PTC's receiver surface receives the concentrated radiations, while the top half is subject to the direct solar beam. It can be seen from Fig. 11b that most of the lost rays that are not received on the receiver are re-reflected on the tube with the aid of the secondary

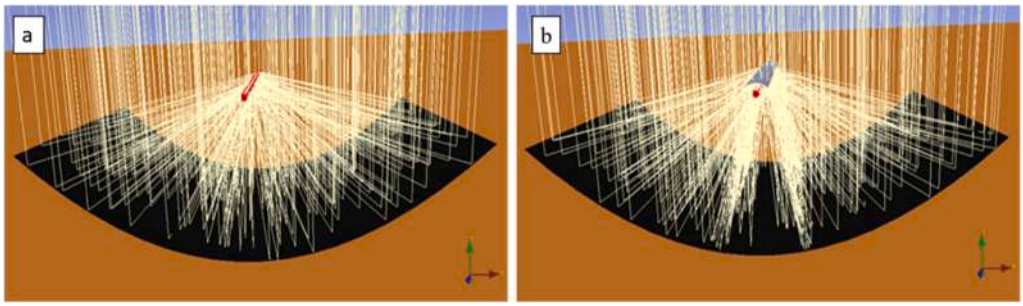

Fig. 11. PTC with concentrated radiations (a) without secondary reflector (b) with secondary reflector.

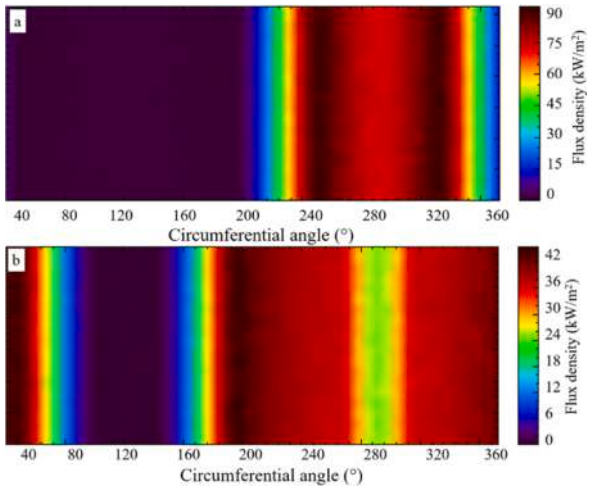

Fig. 12. Radiation flux (W/m^2) in receiver's surface (a) without secondary reflector (b) with secondary reflector.

reflector when the tube is mounted below the focal axis. The heat flux distribution on the receiver tube's outer surface without and with a secondary reflector is demonstrated in Fig. 12a and b, respectively.

It can be observed that the circumferential distribution of radiation flux distribution around the receiver in the PTC without a secondary reflector (Fig. 12a) is exceptionally non-uniform with a large gradient. This non-uniformity in heat flux around the tube wall results in the receiver's deflection, loss of vacuum and leading reasons for PTC failure [41]. On the other hand, the PTC with a secondary reflector can significantly improve the uniformity of heat flux distribution around the receiver with a small gradient, as shown in Fig. 12b. The maximum heat flux of the PTC with and without a secondary reflector is in the range of 42 kW/m^2 and 90 kW/m^2, respectively. As per the design matrix generated by CCD, the ray-tracing numerical analyses are performed on each design point and is explained in the subsequent section.

3.2. Development of model and statistical testing

RSM is the collection of mathematical and statistical techniques such as predictive experimental design procedures, regression modelling techniques and optimisation methods. After the results obtained from MCRT runs, RSM is used for establishing an appropriate model through statistical analysis. The objective of RSM is to choose the most desirable receiver tube misalignment from the primary focal axis and the width of the secondary parabolic reflector based on the uniformity of heat flux and power output of the system. Uniformity is defined as the ratio of the standard deviation of the flux distribution to its mean value. Researchers found that RSM has a significant role in the design, development, and formulations of mathematical models as well as in the enhancements of current systems [42,43]. The eccentricity of the absorber tube from the focal axis of the primary reflector ($f^{'}$) and width of the secondary reflector (W_s) are the key parameters of the PTC system that determine the heat flux distribution and power output. The response surface analysis including four factorial points, four axial points and five replicates at the central points as shown in Table 6 and is applied using central composite design to develop an empirical relationship for predicting heat flux distribution and power output.

Table 6
CCD matrix and results for uniformity and total power.

Run	Factor 1	Factor 2	Response 1	Response 2	Average Heat flux (KW/m^2)
	$f^{'}$ (mm)	W_s (mm)	Uniformity	Total Power (kW)	
1	14.2	70	0.592628	5.56027	0.7943
2	28.1	41.6625	0.82163	2.33787	0.3339
3	28.1	41.6625	0.81487	2.33918	0.3341
4	42.0	13.325	0.887638	1.60674	0.2295
5	14.2	41.6625	0.572282	5.69872	0.8141
6	28.1	13.325	0.791166	2.51064	0.3586
7	28.1	41.6625	0.822295	2.33832	0.3340
8	28.1	41.6625	0.822464	2.33995	0.3342
9	28.1	41.6625	0.822632	2.33896	0.3341
10	42.0	41.6625	0.949518	1.42862	0.2041
11	42.0	70	1.00475	1.28354	0.1833
12	28.1	70	0.853023	2.19612	0.3137
13	14.2	13.325	0.560564	5.84575	0.8351

The stability of the model is tested by using ANOVA. Using the quadratic polynomial model, the final mathematical model for uniformity and total power for the PTC-secondary reflector system obtained is as follows:

$$Uniformity = 0.211873 + 0.028670f^{'} - 0.000186W_s + 0.000027f^{'}W_s - 0.000312f^{'2} + 2.86362E-07W_s^2 \quad (15)$$

$$Totalpower = 11.80149 - 0.503154f^{'} - 0.001310W_s - 0.000123f^{'}W_s + 0.006254f^{'2} - 4.56763E-06W_s^2 + 1.57091E-06f^{'2}W_s + 5.09967E-07f^{'}W_s^2 - 6.63711E-09f^{'2}W_s^2 \quad (16)$$

Table 7
ANOVA for uniformity.

Source	Sum of squares	df	Mean square	F-value	p-value	
Model	0.2286	5	0.0457	2708.44	<0.0001	Significant
A-f'	0.2077	1	0.2077	12307.80	<0.0001	
B-Ws	0.0074	1	0.0074	439.76	<0.0001	
AB	0.0018	1	0.0018	107.14	<0.0001	
A^2	0.0100	1	0.0100	594.49	<0.0001	
B^2	2.337E-06	1	2.337E-06	0.1384	0.7208	
Residual	0.0001	7	0.0000			
Lack of Fit	0.0001	3	0.0000	2.23	0.2271	Not significant
Pure Error	0.0000	4	0.0000			
Cor Total	0.2287	12				

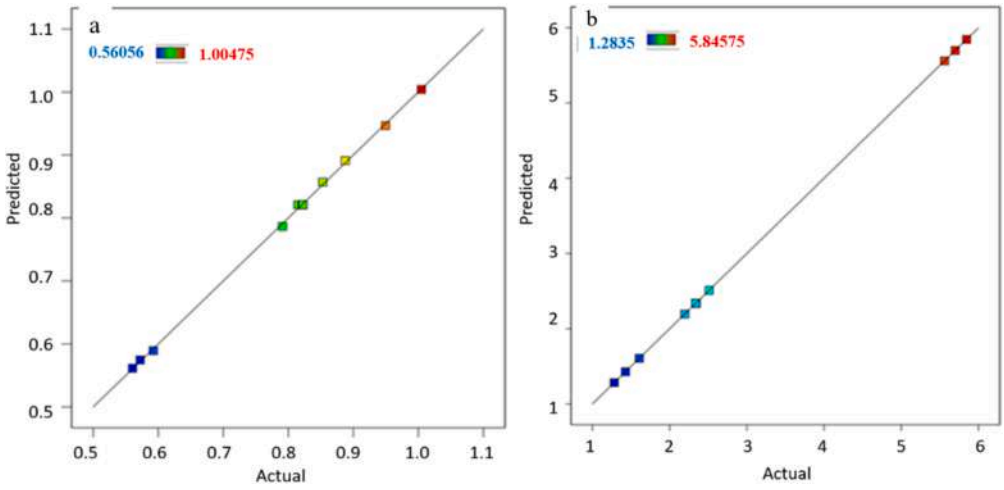

Fig. 13. Experimental results and predicted values (a) uniformity (b) total power.

The ANOVA result for uniformity is illustrated in Table 7. The descriptions of the parameters related to this well-known statistical analysis tool can be found in the literature [44]. The results of the analysis show that factors such as A, B, A^2, and the interaction factor A * B have significant effects in the response surface model of uniformity, where A and B represents $f^{'}$ and W_s, respectively. The F-value of 2707.44 and p-values of <0.001 from the uniformity model indicates the significant model terms. The lack of fit of 2.23 implies that the lack of fit is not substantial, and a non-significant lack of fit is good.

Similarly, from the ANOVA results of the power output, the larger model F-value of 6.271E + 06 and the associated p-values below 0.05 indicate statistical significance for the model terms for the overall power response. The mathematical equations developed can predict the uniformity of heat flux and power output of any PTCs. Fig. 13a and b illustrate the comparison of predicted results of uniformity and total power developed by the RSM with the Tonatiuh results. It is observed that there is an acceptable quantitative and qualitative conformity between predicted and Tonatiuh results.

A confirmation ray-tracing study is also performed for the parameters $f^{'}$ = 29 mm and Ws = 83 mm, and the developed mathematical correlations [Eq. (15) and (16)] and the ray-tracing analysis results are compared, as shown in Table 8. It has been found that the percentage error for uniformity is −0.257 and 1.91 for total power. Hence, the developed models can accurately predict the uniformity and power output of the PTC within the range of investigation.

Table 8
Confirmation between experimental and predicted results.

Response	Experiment result	Predicted result	% error
Uniformity	0.83461	0.83247	−0.257
Total power (kW)	2.2488	2.2066	1.91

3.3. Parametric effects

The individual effects of the receiver tube position ($f^{'}$) and width of the secondary reflector (W_s) on the uniformity of distribution of heat flux over the receiver tube is illustrated in Fig. 14. Uniformity close to zero implies a uniform heat flux distribution around the receiver tube. As shown in Fig. 14a, the receiver tube's location to the primary reflector's focal axis has more influence on the uniformity of heat flux distribution than the secondary reflector width (see Fig. 14b). Due to the receiver tube's significant misalignment, the majority of reflected rays cannot reach the receiver. For the minor deviations of receiver tube locations, the secondary reflector can lead to a more uniform distribution of heat flux over the receiver tube's entire periphery. It can be observed from Fig. 14a that the uniformity of heat flux distribution has improved up to 0.58, while it is 1.0836 for the PTC without secondary reflector, and thus, the achievable improvement factor on heat flux distribution is 1.868.

The combined influence of the receiver tube position ($f^{'}$) and configuration of the secondary reflector (W_s) on the uniformity of distribution of heat flux over the receiver tube is demonstrated using the three-dimensional and contour response surfaces as shown in Fig. 15a and b, respectively. It can be seen that the heat flux distribution becomes non-homogenize when the receiver tube location from the focal axis increases with the increase in width of the secondary collector. Among the thirteen ray-tracing analyses conducted, the heat flux distribution of three configurations is depicted in Fig. 16. As shown in Fig. 16, the distribution of heat flux over the receiver tube periphery follows the same trend as illustrated in Fig. 15. The peak flux of a PTC without a secondary reflector is 90 kW/m^2 (see Fig. 12a). And is reduced to 42

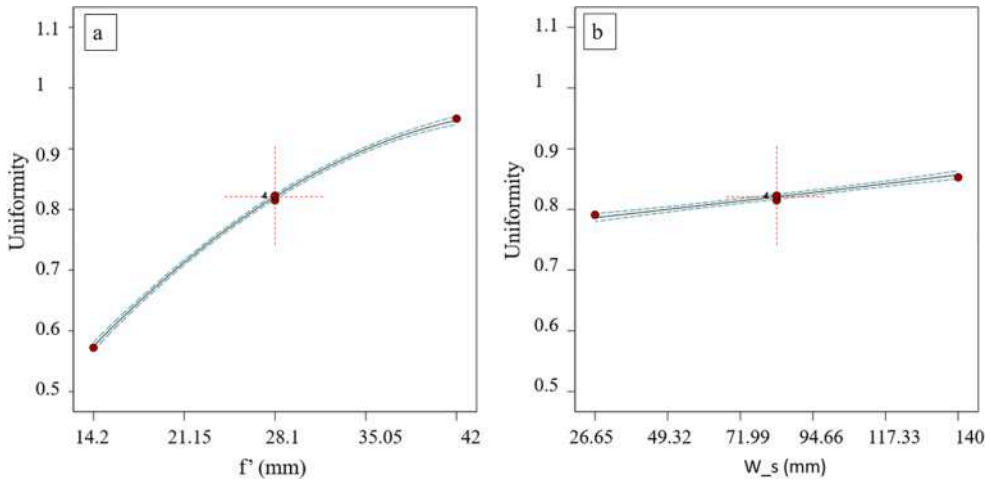

Fig. 14. Uniformity of heat flux distribution with (a) receiver tube position (b) width of the secondary reflector.

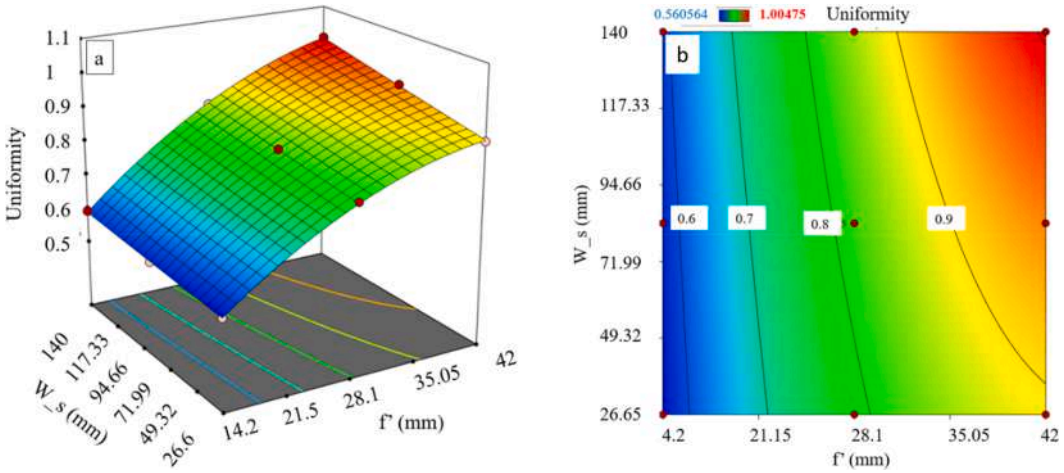

Fig. 15. Interaction effect of receiver position and secondary reflector configuration on heat flux uniformity (a) response surface plot and (b) contour plot.

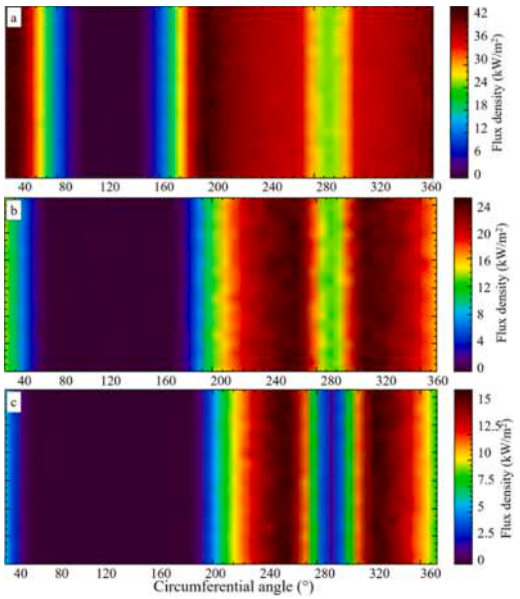

Fig. 16. Distribution of heat flux when (a) f′ = 14.2 mm and Ws = 13.225 mm (b) f′ = 28.1 mm and Ws = 41.6625 mm (c) f′ = 42.0 mm and Ws = 70.0 mm.

kW/m^2 with improved heat flux distribution, as seen in Fig. 16a. The peak heat flux reduction is 73.33%, which is higher than that reported by Reda and Abdelli (70.33%) [35]. The improvement factor of heat flux distribution achieved by Gong et al. [24] design is around two, but it is 1.868 in the current study. Still, the present study uses a parabolic secondary reflector which is simple in construction and economical to incorporate with PTCs rather than the complex multi-parabolic reflector used by Gong et al.

The individual effects of the receiver tube position ($f^{'}$) and configuration of the secondary reflector (W_s) on the power output are illustrated in Fig. 17a and b. Fig. 18a and b show the response surface and contour plots for the combined effect of parameters. The minimum reflector size and deviation of the receiver from the focal axis increase the power output of the system. A non-uniform illumination due to the significant deviation of the receiver tube position and the shading effect of a large secondary reflector on the primary reflector significantly reduces the PTC system's output power.

3.4. Response optimization

A desirability function analysis is performed to identify the most desired parameters [45,46] that improve the uniformity in flux distribution. Placing a secondary reflector above the tube will shadow a portion of the radiation from the primary reflector. This will lead to the reduction in total power received at the reflector. Eventually, a trade-off

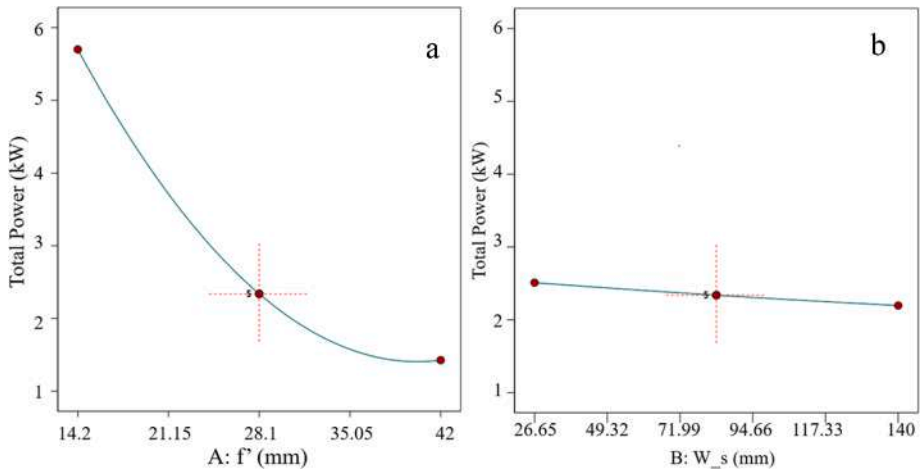

Fig. 17. Effect of power output with (a) receiver tube position and (b) width of secondary collector.

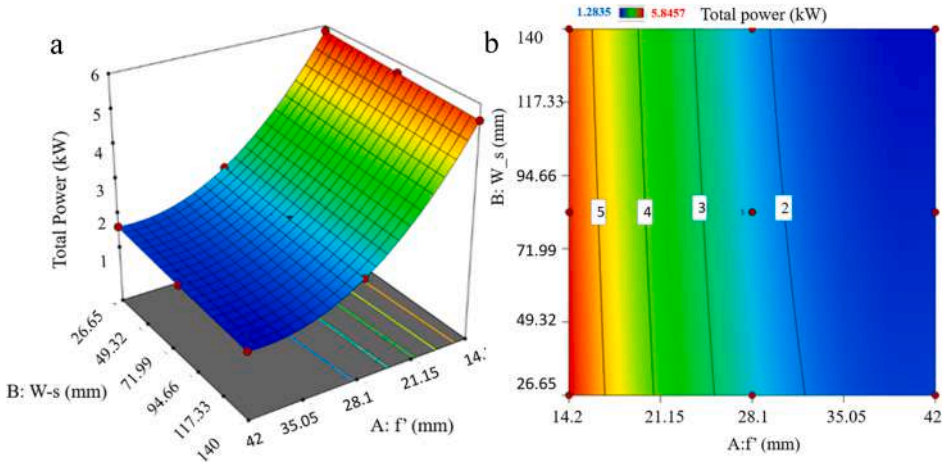

Fig. 18. Interaction effect of receiver position and secondary reflector configuration on power output (a) response surface plot and (b) contour plot.

Table 9
Objectives and constraints for the desirability of parameters and responses.

Factor and response	Goal	Lower limit	Upper limit
Receiver location, f'	In range	14.2	42
Width of sec. reflector, W_s	In range	26.65	140
Uniformity	Minimize	0.560564	1.00475
Power output	Target » 5.5 kW	1.28354	5.84575

is required to choose the desired parameters such that it has better uniformity with very less power loss. This necessitates the objective function (desirability function) with maximising the total power and to minimise the non-uniformity. The set of parameters corresponding to the maximum value of the overall desirability function, subjected to 95% of total output power is identified and selected as the desirable PTC configurations.

To minimise the gradient of heat flux without much effect on the total power, a desirability functional analysis is performed as mentioned above. The optimal level of absorber tube position and the secondary reflector width have been identified. The large flux gradient on the outer tube periphery is the major reason for PTC failures [9]. The optimal level could reduce the circumferential temperature difference on the receiver,

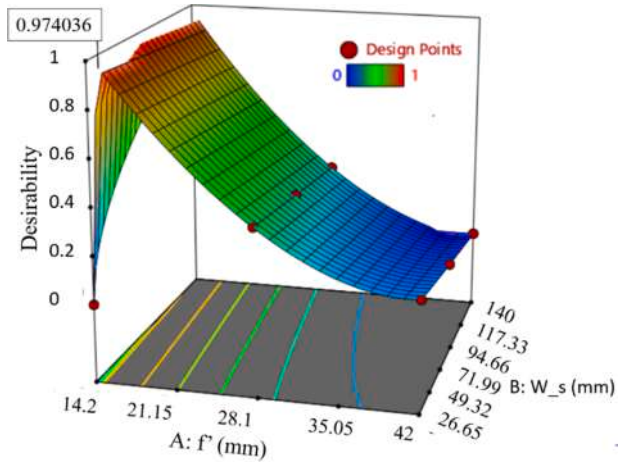

Fig. 19. Response surface plot showing the desirable parameter values.

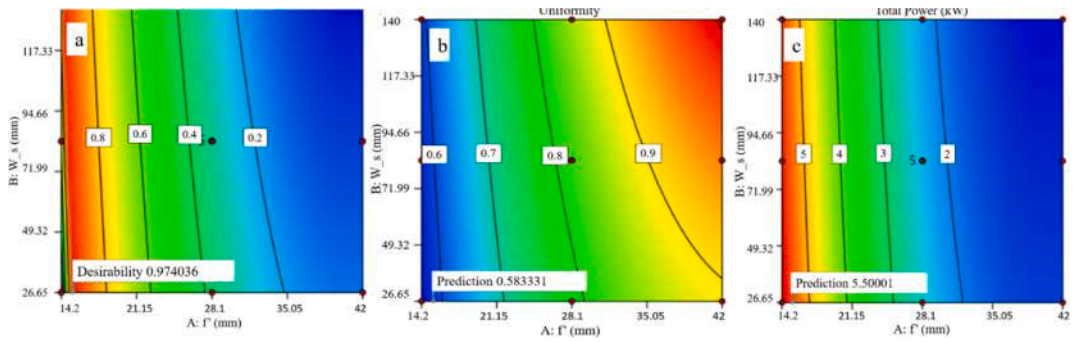

Fig. 20. Contour plots for desirability predictions (a) desirability, (b) uniformity, (c) total power.

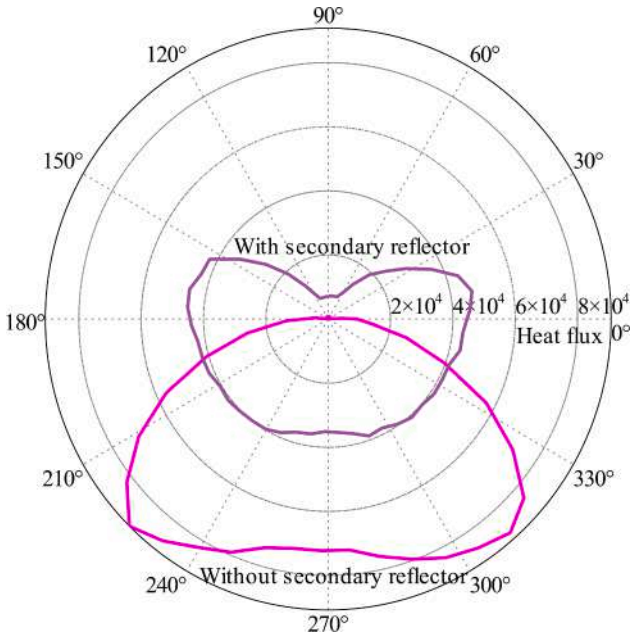

Fig. 21. Heat flux distribution (kW/m^2) on the receiver tube's surface without secondary reflector and with secondary reflector.

thereby improving the reliability and life cycle of the PTC.

Table 9 gives the constraints for desirability for receiver tube position and secondary reflector width. The results of RSM desirability are f' = 15.278 mm and W_s = 26.650 mm and have optimal desirability of 0.974, as depicted in Figs. 19 and 20. The desirability value closer to unity is considered to be the most desirable.

3.5. Computational fluid dynamics (CFD) simulation

A comparative analysis on the thermo-hydraulics of the PTC is performed for the most desirable secondary reflector (Case-I) and the receiver tube without the secondary reflector (Case-II). In order to test for the worst operating condition, the receiver tube alone is considered without the glass cover with a wind velocity of 1 m/s. Fig. 21 depicts the heat flux distribution at the receiver tube's surface without and with the secondary reflector, respectively, as obtained from MCRT analysis. This flux distribution is converted to a profile file and applied as the CFD analysis's heat flux boundary condition.

From Fig. 21, it is observed that the distribution of heat flux for case-II on the bottom side of the receiver is high, and in the upper half, it is null. This is due to most of the radiation reflected directly onto the bottom periphery of the receiver without re-reflection, which leads to the chances of the formation of local hot spots, thermal stresses and hence deformation of the tube. For Case-I, the heat flux distribution on the receiver tube becomes significantly uniform, and the flux gradient reduces. This enhanced heat flux distribution results from re-reflected radiations from the secondary reflector. It is also noted that the polar axis maximum value of the receiver with the secondary reflector is 50 kW/m^2, whereas it is almost 100 kW/m^2 for the receiver without the secondary reflector, as depicted in Fig. 21. This implies that the use of additional reflectors can significantly reduce the peak flux intensity, which avoids the PTC failures due to the uneven heat flux distribution. Thus, the non-uniform distribution of heat flux can be kept at lower levels to ensure the longer service life of the receiver tube with a negligible reduction in fluid temperature.

The temperature distribution on the surface of the receiver with a secondary reflector, as shown in Fig. 23, is considerably more uniform than that of a receiver without a secondary reflector (Fig. 22). A significant reduction in the peak temperature of the wall can be seen from the study. This also signifies the reduction of heat loss from the receiver tube as the radiation loss is of the fourth power of temperature.

The simulation results indicate that for the flow rate of 3 lpm, the peak temperature obtained at the surface of the receiver with a secondary reflector is 90.6 °C, and that of the receiver without the secondary reflector is 111 °C. The corresponding bulk mean temperatures of the fluid at the outlet are 65.8 °C and 68.8 °C, respectively. Even though the maximum wall temperature of the receiver tube with the secondary reflector is around 20 °C less than that of the receiver positioned at the actual focal axis without a reflector, the difference in bulk

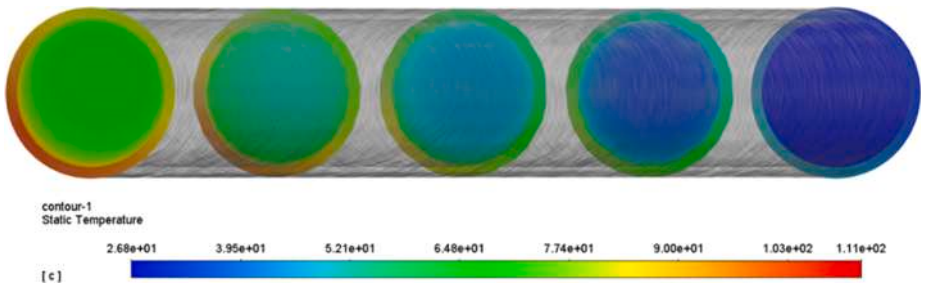

Fig. 22. Temperature contour at different cross sections of the receiver tube without secondary reflector for 3 lpm.

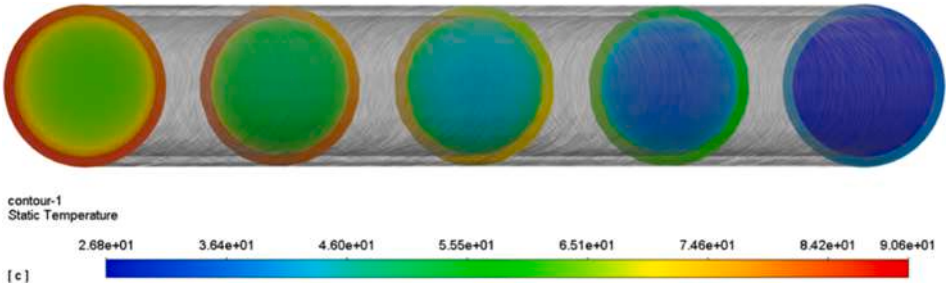

Fig. 23. Temperature contour at different cross sections of the receiver tube with secondary reflector for 3 lpm.

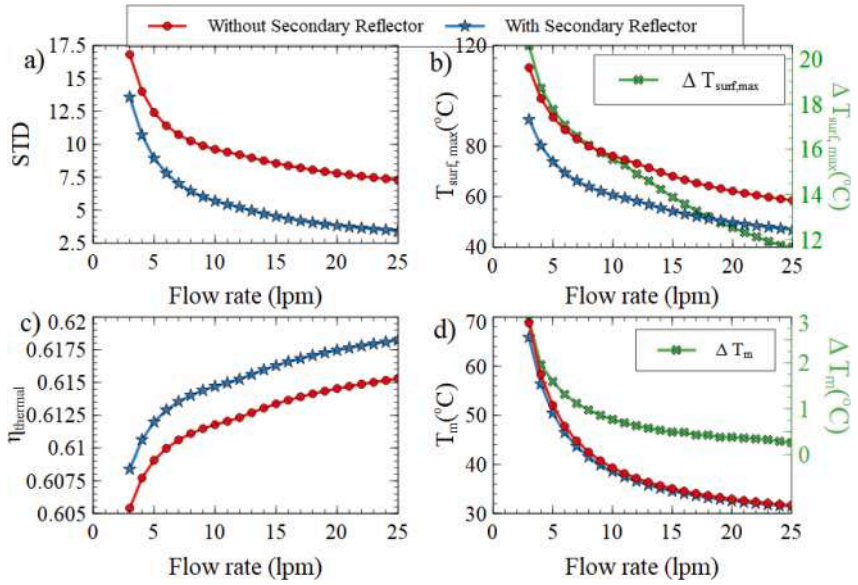

Fig. 24. Variation of the performance indices considered in the study.

mean temperature is only 3 °C. The same trend of improving the circumferential distribution of heat flux accompanied by a slight fluid temperature reduction was reported in the literature [9].

3.5.1. Comparative study of PTC with and without secondary reflector

A detailed performance analysis is carried out to provide further insight into the influence of the secondary reflector on the heat flux distribution and efficiency of the PTC. The flow rate varies from 3 to 25 lpm is considered for the present study. The temperature distribution around the receiver tube, maximum receiver surface temperature ($T_{surf,max}$), bulk mean fluid temperature (T_m) at the outlet, and thermal efficiency of the PTC with and without secondary reflector are investigated. Fig. 24 depicts the performance indices utilised in the comparative study. STD denotes the standard deviation of the temperature distribution around the receiver tube. This rating indicates the degree to which temperature is uniform. The receiver with a secondary reflector exhibits a more uniform temperature distribution at all flow rates evaluated.

Additionally, as the flow rate increases, the STD value for the receiver with secondary reflector reduces significantly faster than for the receiver without the secondary reflector (Fig. 24a). At lower flow rate, the difference in peak surface temperature between the PTC without and with secondary reflector is 20 °C, whereas it is reduced to 12 °C for the higher flow rate as depicted in Fig. 24(b). This has the added benefit of minimising heat transfer losses from the receiver tube. This temperature differential reduces as the flow rate increases, but the 12 °C difference at the maximum design flow rate is significant. Due to the fact that the bulk mean temperature remains constant in both cases, the receiver with secondary reflector has a very slight increase in thermal efficiency ($\eta_{thermal}$) of about 0.05 percent (Fig. 24c). The thermal efficiency is determined by using Eq. (17). The increase in thermal efficiency is significant in the case of PTCs with extremely long receiver tube sections, such as those used in thermal power plants. The most intriguing discovery concerns the bulk mean temperature.

$$\eta_{thermal} = \frac{\dot{m}C_p(T_{out} - T_{in})}{q_{Total}} \tag{17}$$

The exergetic efficiency is also evaluated using the methodology detailed by Bellos et al. [47]. Here the exergy flow of the solar irradiation is evaluated using the equation,

$$E_s = Q_s\left[1 - \frac{4}{3}\left(\frac{T_{am}}{T_{sun}}\right) + \frac{1}{3}\left(\frac{T_{am}}{T_{sun}}\right)^4\right] \tag{18}$$

where T_{sun}, is the temperature of the sun, which is estimated as 5770 K, Q_s , being the total heat available in Joules. The useful exergy output is calculated according the following equation,

$$E_u = Q_u - mC_pT_{am}\ln\left(\frac{T_{out}}{T_{in}}\right) - mT_{am}\frac{\Delta P}{\rho_{water}T_{water}} \tag{19}$$

Since the pressure drop for a length of 2.5 m as per the work is negligible, the third term in the right hand side is neglected. With this, the exergetic efficiency is evaluated as, $\eta_{ex} = \frac{E_u}{E_s}$. A similar trend is obtained for exergetic efficiency as for the thermal efficiency. For the case without secondary reflector, η_{ex}, varies from 0.56 to 0.60 while for the case with secondary reflector it is 0.57–0.61 with the mass flux. The improvement in exergy efficiency is also marginal in the range of 0.1%

at low mass flow rate and 0.05% at high mass flow rate. This behaviour is predictable from the results portrayed in the Fig. 24.

Although the overall heat flux value is reduced by 6% due to the secondary reflector's shade, the bulk mean temperature, which indicates the energy intensity of the water at the outlet, is consistent for both receivers. At a low flow rate of 3 lpm, the maximum temperature difference is 3 °C, while it is 0.25 °C at a maximum flow rate of 25 lpm (Fig. 24d). This is essentially trivial, given the variation between the two scenarios is only around 0.8 per cent. In reality, the receiver tube of a traditional PTC encountered severe non-uniform heat flux, resulting in the loss of a significant amount of the radiations. This radiation loss may further drop the outlet temperature of the convectional receiver down below that of the receiver tube's HTF when a secondary reflector is used. Additionally, receiver deflection is a significant cause of PTC failures and affects the reliability and lifetime of the PTCs [9]. As a result, the design and application of a secondary reflector can be seen as a necessary choice.

4. Conclusions

This paper investigates a new parabolic trough solar collector design strategy that uses a secondary parabolic reflector to homogenise the concentrated solar flux distribution on the receiver tube and achieve a uniform flux distribution with the appropriate total power.

The following findings can be drawn from the current research.

- By homogenising the flux distribution, secondary reflector parabolic trough collector systems can be configured to meet the required output power as well as the system's prolonged service life.
- The system's performance is investigated by developing a comprehensive procedure that uses central composite design, Monte Carlo ray-tracing, response surface methodology, analysis of variance, and computational fluid dynamics to efficiently build the system with the most desirable parameters.
- A uniformity value of 0.58 is attained with the secondary reflector in its most desired placement. It is 1.0836 for the receiver without a secondary reflector. The heat flux distribution is enhanced by a factor of 1.868.
- The computational fluid dynamics analysis confirms that the heat transfer fluid's average outlet temperature is not considerably affected despite reducing total power. Furthermore, because the flux is dispersed more evenly, the possibility of a hot spot, where the local peak temperature rises dramatically, is reduced. Peak surface temperature can be decreased, and heat loss due to convection and radiation can be considerably reduced by homogenising the flux.
- The new design significantly improved the heat flux distribution of the receiver with comparable thermal efficiency.
- Models for uniformity and power output have been developed that are independent of the primary collector and can be applied to any PTC.
- This step-by-step technique introduces a new design approach for establishing the receiver tube position and secondary reflector configuration in order to achieve consistent heat flux distribution and solar collector power output.
- The studies of parabolic trough collector with a secondary reflector described above are extremely useful in creating actual systems and providing a better knowledge of the design of optimum parabolic solar collectors.

Declaration of Competing Interest

The authors declare that they have no known competing financial interests or personal relationships that could have appeared to influence the work reported in this paper.

References

[1] A. Fernández-García, E. Zarza, L. Valenzuela, M. Pérez, Parabolic-trough solar collectors and their applications, Renew. Sustain. Energy Rev. 14 (7) (2010) 1695–1721, https://doi.org/10.1016/j.rser.2010.03.012.

[2] A.S. Tijani, A.M.S. Bin Roslan, Simulation analysis of thermal losses of parabolic trough solar collector in malaysia using computational fluid dynamics, Proc. Technol. 15 (2014) 841–848, https://doi.org/10.1016/j.protcy.2014.09.058.

[3] M. Jradi, S. Riffat, Medium temperature concentrators for solar thermal applications, Int. J. Low-Carbon Technol. 9 (3) (2014) 214–224, https://doi.org/10.1093/ijlct/cts068.

[4] M.E. Argun, A.A. Kulaksız, Performance investigation of a new solar desalination unit based on sequential flat plate and parabolic dish collector, Int. J. Green Energy 14 (6) (2017) 561–568, https://doi.org/10.1080/15435075.2017.1310106.

[5] W. Gao, G. Xu, T. Li, H. Li, Modeling and performance evaluation of parabolic trough solar cavity-type receivers, Int. J. Green Energy 12 (12) (2015) 1263–1271, https://doi.org/10.1080/15435075.2014.909356.

[6] A.A. Hachicha, I. Rodríguez, R. Capdevila, A. Oliva, Heat transfer analysis and numerical simulation of a parabolic trough solar collector, Appl. Energy 111 (2013) 581–592, https://doi.org/10.1016/j.apenergy.2013.04.067.

[7] S.M. Jeter, The distribution of concentrated solar radiation in paraboloidal collectors, J. Sol. Energy Eng. Trans. ASME. 108 (1986) 219–225, https://doi.org/10.1115/1.3268096.

[8] D. Zhao, E. Xu, Q. Yu, D. Lei, The simulation model of flux density distribution on an absorber tube, Energy Proc. 69 (2015) 250–258, https://doi.org/10.1016/j.egypro.2015.03.029.

[9] K. Wang, YaLing He, ZeDong Cheng, A design method and numerical study for a new type parabolic trough solar collector with uniform solar flux distribution, Sci. China Technol. Sci. 57 (3) (2014) 531–540, https://doi.org/10.1007/s11431-013-5452-6.

[10] M. Wirz, M. Roesle, A. Steinfeld, Three-dimensional optical and thermal numerical model of solar tubular receivers in parabolic trough concentrators, J. Sol. Energy Eng. 134 (2012) 041012, https://doi.org/10.1115/1.4007494.

[11] V. Khullar, P. Mahendra, M. Mittal, Applicability of heat mirrors in reducing thermal losses in concentrating solar collectors, J. Therm. Sci. Eng. Appl. 10 (2018) 061004, https://doi.org/10.1115/1.4040653.

[12] B. El Ghazzani, D. Martinez Plaza, R. Ait El Cadi, A. Ihlal, B. Abnay, K. Bouabid, Thermal plant based on parabolic trough collectors for industrial process heat generation in Morocco, Renew. Energy 113 (2017) 1261–1275, https://doi.org/10.1016/j.renene.2017.06.063.

[13] M.C. Kulahli, S. Akbulut Özen, A.B. Etemoglu, Numerical simulation of a parabolic trough collector containing a novel parabolic reflector with varying focal length, Appl. Therm. Eng. 161 (2019) 114210, https://doi.org/10.1016/j.applthermaleng.2019.114210.

[14] X. Wang, S. Luo, T. Tang, X. Liu, Y. He, A MCRT-FVM-FEM coupled simulation for optical-thermal-structural analysis of parabolic trough solar collectors, Energy Proc. 158 (2019) 477–482, https://doi.org/10.1016/j.egypro.2019.01.138.

[15] B. Zou, H. Yang, Y. Yao, Y. Jiang, A detailed study on the effects of sunshape and incident angle on the optical performance of parabolic trough solar collectors, Appl. Therm. Eng. 126 (2017) 81–91, https://doi.org/10.1016/j.applthermaleng.2017.07.149.

[16] B. Kurşun, Thermal performance assessment of internal longitudinal fins with sinusoidal lateral surfaces in parabolic trough receiver tubes, Renew. Energy. 140 (2019) 816–827, https://doi.org/10.1016/j.renene.2019.03.106.

[17] Z. Zhao, F. Bai, X. Zhang, Z. Wang, Experimental study of pin finned receiver tubes for a parabolic trough solar air collector, Sol. Energy. 207 (2020) 91–102, https://doi.org/10.1016/j.solener.2020.06.070.

[18] Y. Xu, Q. Ren, Z. Zheng, Y. He, Evaluation and optimization of melting performance for a latent heat thermal energy storage unit partially filled with porous media, Appl. Energy. 193 (2017) 84–95, https://doi.org/10.1016/j.apenergy.2017.02.019.

[19] S. Ebrahim Ghasemi, A. Akbar Ranjbar, Numerical thermal study on effect of porous rings on performance of solar parabolic trough collector, Appl. Therm. Eng. 118 (2017) 807–816, https://doi.org/10.1016/j.applthermaleng.2017.03.021.

[20] B.N. Kumar, K.S. Reddy, Numerical investigations on metal foam inserted solar parabolic trough DSG absorber tube for mitigating thermal gradients and enhancing heat transfer, Appl. Therm. Eng. 178 (2020) 115511, https://doi.org/10.1016/j.applthermaleng.2020.115511.

[21] M.T. Jamal-Abad, S. Saedodin, M. Aminy, Experimental investigation on a solar parabolic trough collector for absorber tube filled with porous media, Renew. Energy. 107 (2017) 156–163, https://doi.org/10.1016/j.renene.2017.02.004.

[22] A. Bharti, A. Mishra, B. Paul, Thermal performance analysis of small-sized solar parabolic trough collector using secondary reflectors, Int. J. Sustain. Energy. 38 (10) (2019) 1002–1022, https://doi.org/10.1080/14786451.2019.1613991.

[23] E. Bellos, C. Tzivanidis, Investigation of a booster secondary re fl ector for a parabolic trough solar collector, Sol. Energy. 179 (2019) 174–185, https://doi.org/10.1016/j.solener.2018.12.071.

[24] J.-h. Gong, J. Wang, P.D. Lund, E.-y. Hu, Z.-C. Xu, G.-P. Liu, G.-S. Li, Improving the performance of a 2-stage large aperture parabolic trough solar concentrator using a secondary reflector designed by adaptive method, Renew. Energy 152 (2020) 23–33, https://doi.org/10.1016/j.renene.2020.01.019.

[25] E. Bellos, C. Tzivanidis, Alternative designs of parabolic trough solar collectors, Prog. Energy Combust. Sci. 71 (2019) 81–117, https://doi.org/10.1016/j.pecs.2018.11.001.

[26] M. Abdelhamid, B.K. Widyolar, L. Jiang, R. Winston, E. Yablonovitch, G. Scranton, D. Cygan, H. Abbasi, A. Kozlov, Novel double-stage high-concentrated solar hybrid

photovoltaic/thermal (PV/T) collector with nonimaging optics and GaAs solar cells reflector, Appl. Energy. 182 (2016) 68–79, https://doi.org/10.1016/j.apenergy.2016.07.127.
[27] D. Rodriguez-sanchez, G. Rosengarten, Improving the concentration ratio of parabolic troughs using a second-stage flat mirror, Appl. Energy. 159 (2015) 620–632, https://doi.org/10.1016/j.apenergy.2015.08.106.
[28] A. Minaeian, A. Alemrajabi, M. Chavoshi, A. Mostafaeipour, Z. Seifi, Effect of secondary reflector on solar flux intensity and uniformity of a Fresnel concentrator, J. Renew. Sustain. Energy. 12 (2020) 033703, https://doi.org/10.1063/5.0007604.
[29] X.Y. Tang, W.W. Yang, Y. Yang, Y.H. Jiao, T. Zhang, A design method for optimizing the secondary reflector of a parabolic trough solar concentrator to achieve uniform heat flux distribution, Energy 229 (2021) 120749, https://doi.org/10.1016/j.energy.2021.120749.
[30] M. Hack, G. Zhu, T. Wendelin, Evaluation and comparison of an adaptive method technique for improved performance of linear Fresnel secondary designs, Appl. Energy 208 (2017) 1441–1451, https://doi.org/10.1016/j.apenergy.2017.09.009.
[31] S. Balaji, K.S. Reddy, T. Sundararajan, Optical modelling and performance analysis of a solar LFR receiver system with parabolic and involute secondary reflectors, Appl. Energy 179 (2016) 1138–1151, https://doi.org/10.1016/j.apenergy.2016.07.082.
[32] M. Marefati, M. Mehrpooya, M.B. Shafii, Optical and thermal analysis of a parabolic trough solar collector for production of thermal energy in different climates in Iran with comparison between the conventional nanofluids, J. Clean. Prod. 175 (2018) 294–313, https://doi.org/10.1016/j.jclepro.2017.12.080.
[33] C.M. Ghodbane, B. Boumeddane, Engineering design and optical investigation of a concentrating collector: case study of a parabolic trough, J. Fundam. Appl. Sci. 10 (2018) 148–171, https://doi.org/10.4314/jfas.v10i2.11.
[34] S. Wu, R. Tang, C. Wang, Numerical calculation of the intercept factor for parabolic trough solar collector with secondary mirror, Energy 233 (2021) 121175, https://doi.org/10.1016/j.energy.2021.121175.
[35] H.M. Reda, B. Abdelylah, Numerical investigation and solar flux distribution analysis of parabolic trough solar collector by adding secondary reflector, Instrum. Mes. Metrol. 18 (2019) 275–280. doi:10.18280/i2m.180307.
[36] T. Osório, P. Horta, M. Larcher, R. Pujol-nadal, J. Hertel, D.W. Van Rooyen, S. Schneider, D. Benitez, A. Frein, A. Denarie, T. Osório, P. Horta, M. Larcher, R. Pujol-nadal, Ray-tracing software comparison for linear focusing solar collectors, AIP Conf. Proc. 1734 (2016), https://doi.org/10.1063/1.4949041.
[37] F. Chen, M. Li, P. Zhang, Distribution of energy density and optimization on the surface of the receiver for parabolic trough solar concentrator, Int. J. Photoenergy. 2015 (2015) 1–10, https://doi.org/10.1155/2015/120917.
[38] Y. Wang, D. Potter, C.A. Asselineau, C. Corsi, M. Wagner, C. Caliot, B. Piaud, M. Blanco, J.S. Kim, J. Pye, Verification of optical modelling of sunshape and surface slope error for concentrating solar power systems, Sol. Energy. 195 (2020) 461–474, https://doi.org/10.1016/j.solener.2019.11.035.
[39] S. Mathew, G. Visavale, CFD Analysis of a Heat Collector Element in a Solar Parabolic Trough Collector (2014) 1–21. doi:10.13140/2.1.3247.4241.
[40] J.P. Abraham, E.M. Sparrow, W.J. Minkowycz, Internal-flow Nusselt numbers for the low-Reynolds-number end of the laminar-to-turbulent transition regime, Int. J. Heat Mass Transf. 54 (1-3) (2011) 584–588, https://doi.org/10.1016/j.ijheatmasstransfer.2010.09.012.
[41] J. Li, Z. Wang, J. Li, D. Lei, Vacuum reliability analysis of parabolic trough receiver, Sol. Energy Mater. Sol. Cells. 105 (2012) 302–308, https://doi.org/10.1016/j.solmat.2012.06.034.
[42] M. Hatami, J. Geng, D. Jing, Enhanced efficiency in Concentrated Parabolic Solar Collector (CPSC) with a porous absorber tube filled with metal nanoparticle suspension, Green Energy Environ. 3 (2) (2018) 129–137, https://doi.org/10.1016/j.gee.2017.12.002.
[43] I.A. Rauf, P. Rezai, A review of materials selection for optimized efficiency in quantum dot sensitized solar cells: a simplified approach to reviewing literature data, Renew. Sustain. Energy Rev. 73 (2017) 408–422, https://doi.org/10.1016/j.rser.2017.01.137.
[44] A.F. Siegel, Chapter 15 – ANOVA: Testing for Differences among Many Samples, and Much More, Sixth Edit, Andrew F. Siegel, 2012. doi:10.1016/B978-0-12-385208-3.00015-8.
[45] A. Yüksel, Utilization of response surface methodology in optimization of of extraction extraction of optimization of plant plant materials, in: Stat. Approaches With Emphas. Des. Exp. Appl. to Chem. Process. Range, 2018, pp. 157–169. doi:10.5772/intechopen.73690.
[46] V. Sarabhai, S. Centre, J. Joseph, T. Selvaraj, D. Sivakumar, Application of desirability-function and RSM to optimise the multi-objectives while turning Inconel 718 using coated carbide tools application of desirability-function and RSM to optimise the multi-objectives while turning Inconel 718 using coated carbide, Int. J. Manuf. Technol. Manag. 27(4/5/6) (2013) 218–237. doi:10.1504/IJMTM.2013.058899.
[47] E. Bellos, C. Tzivanidis, A detailed exergetic analysis of parabolic trough collectors, Energy Convers Manag. 149 (2017) 275–292, https://doi.org/10.1016/j.enconman.2017.07.035.